

# Modeling and simulations of the spreading and destabilization of nematic droplets

L. J. Cummings, T.-S. Lin, L. Kondic

*Department of Mathematical Sciences and Center for Applied Mathematics and Statistics  
New Jersey Institute of Technology, Newark, NJ 07102*

(Dated: February 26, 2011)

A series of experiments [C. Poulard & A.M. Cazabat, “Spontaneous spreading of nematic liquid crystals,” *Langmuir* 21, 6270-6276 (2005)] on spreading droplets of nematic liquid crystal (NLC) reveal a surprisingly rich variety of behaviors. Small droplets can either be arrested in their spreading, spread stably, destabilize without spreading (corrugated surface), or spread with a fingering instability and corrugated free surface. In this work, we discuss the problem of NLC drops spreading in a simplified two-dimensional (2D) geometry. The model that we present is based on a long-wavelength approach for NLC’s due to Ben Amar & Cummings [M. Ben Amar & L.J. Cummings, “Fingering instabilities in driven thin nematic films,” *Phys. Fluids* 13, 1160-1166 (2001), L.J. Cummings, “Evolution of a thin film of nematic liquid crystal with anisotropic surface energy,” *Europ. J. Appl. Math.* 15, 651-677 (2004)]. The improvements of the model here permit fully nonlinear time-dependent simulations. These simulations, for the appropriate choice of parameter values, exhibit 2D versions of most of the phenomena mentioned above.

## I. INTRODUCTION

In a series of beautiful and surprising experiments in 2005, Poulard & Cazabat observed remarkable spontaneous instabilities in droplets of nematic liquid crystal (5CB, pentyl-cyanobiphenyl) spreading on hydrophilic silicon substrates under conditions of high relative humidity [1]. Some experimental photographs from that paper are reproduced in Fig. 1, illustrating the wide range of possible droplet behaviors that was found (at large times) as experimental conditions were varied. The authors found that the drops could either remain stable without spreading (Fig. 1(a)), spread stably (Fig. 1(b)), or spread while destabilizing (Figs. 1(c), (d), (e), which show the late stages of such instabilities). The major factors influencing the behavior appear to be the relative humidity (RH) at which the experiment is carried out, and the droplet size: qualitatively speaking, at low RH ( $< 40\%$ ) no spreading is observed, Fig. 1(a); at intermediate RH ( $40\% < \text{RH} < 60\%$ ) stable spreading is seen, Fig. 1(b); for  $60\% < \text{RH} < 80\%$  instabilities develop at the moving contact line, (and in the free upper surface of the droplet) Fig. 1(c); and for  $\text{RH} > 80\%$  a second (longer wavelength) instability is manifested, Fig. 1(d). In general, small droplets are reported to be stable however, even at high RH; while larger droplets can be unstable as observed above. Curiously, all contact line instabilities are observed to fade away at very large times, as spreading ceases.

We note also experimental data of Bénichou *et al.* [2] on a similar system: small droplets of *n*CB liquid crystal are allowed to spread on oxidized silicon wafers, and the profiles of the spreading drops obtained via ellipsometry measurements. Typical experimental results are illustrated in Fig. 2 for the liquid crystal 9CB. Although the experimental profiles in that paper are obtained for *n*CB in the smectic phase (rather than the nematic), and the droplet height in these experiments is very much smaller than in the experiments of [1] (so that the appropriate

scalings are quite different), the basic instability mechanism we propose in this paper (driven by internal elasticity) should be applicable here also. In the present paper, however, we focus on the scalings appropriate for the experiments of Poulard & Cazabat [1], deferring a detailed consideration of the terraced spreading and free surface shapes of Fig. 2 to a separate investigation.

As is apparent, despite the simplicity of the experimental setup, the observed behavior is remarkably complex, and our challenge is to find a minimal plausible model capable of exhibiting such behavior in different parameter regimes. The model we derive does not account for the presence (or effect) of defects in the nematic director field; but Poulard & Cazabat note that defects are present in their experiments [1], and speculate that the instabilities may be linked to them. This could certainly be the case; however, our model nonetheless suggests that at least some of the observations can be explained with a defect-free model.

## II. THE MODEL

Throughout this paper we restrict attention to the 2D case for simplicity. A model for 3D droplet behavior will be analyzed in a separate publication. The main dependent variables governing the dynamics of a liquid crystal in the nematic phase are the velocity field  $\mathbf{v} = (v_1, 0, v_3) = (u, 0, w)$ , and director field  $\mathbf{n} = (\sin \theta, 0, \cos \theta)$ , the unit vector describing the orientation of the anisotropic axis in the liquid crystal (an idealized representation of the local preferred average direction of the rod-like liquid crystal molecules). The director angle  $\theta(x, z, t)$  is a function of space and time, determined by minimizing a suitably-defined free energy  $W$  within the NLC, with coupling to the local flow-field. Molecules like to align locally, and this preference is modeled by an elastic energy, which is minimized subject to boundary constraints. In general, a bounding surface is

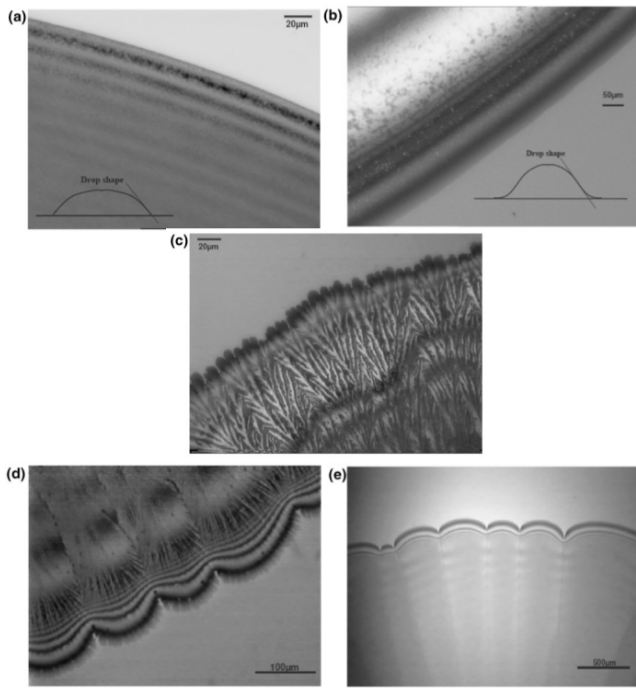


FIG. 1: Experimental photos reproduced from Poulard & Cazabat [1]. Full details are given in [1], but in summary, (a) shows a stable, non-spreading droplet of 5CB at 20% relative humidity (RH); (b) shows a stable spreading droplet at 50% RH; (c) shows a spreading unstable droplet at 80% RH, with corrugated free surface and fingering at the apparent contact line; and (d) shows another unstable spreading droplet at yet higher RH 90%. In (d) a second, longer-wavelength instability appears alongside the first, and in (e) only this second instability is present.

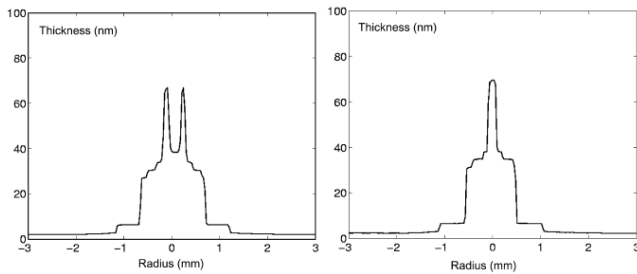


FIG. 2: Ellipsometric data reproduced from Bénichou *et al.* [2], showing large-time profiles (400 and 1000 minutes, respectively) of spreading droplets of 9CB on silicon wafers. Full details in [2].

associated with a given preferred direction for  $\mathbf{n}$ ; this preference is known as surface anchoring. Anchoring can be tuned by appropriate (chemical or mechanical) treatment of a surface (for example, it is known that rubbing a glass surface with a cloth can impart so-called parallel or planar anchoring; the rubbing etches microscopic grooves in the surface, in which the rod-like molecules like to lie),

and may be either weak or strong. Strong anchoring is simply modeled by a Dirichlet condition on the director field, while weak anchoring is most commonly modeled by assigning a surface energy (such as Rapini-Papoular [3]) with given anchoring strength to the boundary.

Our starting-point is a model first presented by Ben Amar & Cummings [4] (and later extended by Cummings [5]) for flow of a thin film of nematic liquid crystal on a solid surface, under surface tension and gravity, with strong anchoring conditions imposed on the director at both the substrate and the free surface. We outline the theory for a 2D drop with free surface  $z = h(x, t)$  (or  $x_3 = h(x_1, t)$ ) noting that the model is easily extended to a 3D drop with surface  $z = h(x, y, t)$ . In the so-called “lubrication” limit in which the film thickness is much smaller than typical lengthscales of flow variations in the plane of the substrate, the governing Leslie-Ericksen equations simplify dramatically. With a slowly-deforming droplet and strong anchoring conditions, the energy equation decouples from the flow, and reduces to the Euler-Lagrange minimization of the elastic energy of the liquid crystal for the instantaneous drop geometry, with director angles specified at both upper (free) and lower (fixed) surfaces. With the assumed slender drop geometry this is particularly simple: the director angle is a linear function of the coordinate  $z$  (or  $x_3$ ) perpendicular to the substrate, and assumes the specified anchoring angles at upper and lower surfaces. If the difference in these anchoring angles is  $\Delta\Theta \neq 0$  then with strong anchoring the director angle is forced to bend through an angle  $\Delta\Theta$  across the film thickness,  $h$ . While  $h$  is not too small this is possible; but as  $h$  gets small (e.g. a thinning film, or, in the extreme case, as a contact line is approached) the associated energy diverges, and the film prefers to corrugate.

This is the basic instability mechanism proposed by Ben Amar & Cummings [4]; and whilst we believe the argument is essentially valid, the strong anchoring model is only satisfactory for a relatively thick film, and it certainly cannot accurately describe the situation near a contact line (moving or otherwise), where there is a complete mismatch between the director angles. In this paper we therefore propose to relax the strong anchoring so that as the film thickness gets very small, the director does not have to bend through the fixed angle  $\Delta\Theta$  but can bend through a smaller angle, which in fact goes to zero as  $h \rightarrow 0$ .

For simplicity in the model derivation, we neglect inertia (of both fluid and director) from the outset, noting that the drops spread very slowly. The Ericksen-Leslie equations for the flow of a nematic liquid crystal, using standard notation (with indices running over  $i = 1, 3$  in

this 2D case) are then:

$$\frac{\partial}{\partial x_i} \left( \frac{\partial W}{\partial \theta_{x_i}} \right) - \frac{\partial W}{\partial \theta} + \tilde{g}_i \frac{\partial n_i}{\partial \theta} = 0, \quad (1)$$

$$-\frac{\partial \pi}{\partial x_i} + \tilde{g}_k \frac{\partial n_k}{\partial \theta} + \frac{\partial \tilde{t}_{ik}}{\partial x_k} = 0, \quad (2)$$

$$\frac{\partial v_i}{\partial x_i} = 0, \quad (3)$$

(see, *e.g.*, [6–8]) representing energy, momentum, and mass conservation, respectively. The quantities  $\tilde{\mathbf{g}} = (\tilde{g}_i)$  and  $\pi$  are defined by

$$\tilde{g}_i = -\gamma_1 N_i - \gamma_2 e_{ik} n_k, \quad e_{ij} = \frac{1}{2} \left( \frac{\partial v_i}{\partial x_j} + \frac{\partial v_j}{\partial x_i} \right), \quad (4)$$

$$N_i = \dot{n}_i - \omega_{ik} n_k, \quad \omega_{ij} = \frac{1}{2} \left( \frac{\partial v_i}{\partial x_j} - \frac{\partial v_j}{\partial x_i} \right), \quad (5)$$

$$\pi = p + W, \quad (6)$$

where  $\gamma_1$  and  $\gamma_2$  are constant viscosities, and  $p$  is the pressure; an over-dot denotes differentiation with respect to time  $t$ ; and  $W$  is the bulk elastic energy, defined by

$$2W = K_1 (\nabla \cdot \mathbf{n})^2 + K_2 (\mathbf{n} \cdot \nabla \times \mathbf{n})^2 + K_3 ((\mathbf{n} \cdot \nabla) \mathbf{n}) \cdot ((\mathbf{n} \cdot \nabla) \mathbf{n}) \quad (7)$$

where  $K_1$ ,  $K_2$  and  $K_3$  are elastic constants (in the 2D model the term in  $K_2$  vanishes identically). Finally,  $\tilde{t}_{ij}$  is the extra-stress tensor (related to the stress  $\sigma_{ij}$  by  $\sigma_{ij} = -\pi \delta_{ij} + \tilde{t}_{ij}$ ), given by

$$\begin{aligned} \tilde{t}_{ij} = & \alpha_1 n_k n_p e_{kp} n_i n_j + \alpha_2 N_i n_j + \alpha_3 N_j n_i + \alpha_4 e_{ij} \\ & + \alpha_5 e_{ik} n_k n_j + \alpha_6 e_{jk} n_k n_i, \end{aligned} \quad (8)$$

where  $\alpha_i$  are constant viscosities (related to the  $\gamma_i$  in (4) by  $\gamma_1 = \alpha_3 - \alpha_2$ ,  $\gamma_2 = \alpha_6 - \alpha_5$ , and to each other by the ‘Onsager’ relation  $\alpha_2 + \alpha_3 = \alpha_6 - \alpha_5$ ) though they are not necessarily all positive, and  $\mu = \alpha_4/2 > 0$  corresponds to the usual viscosity in the standard Newtonian (isotropic) case when all other  $\alpha_i$  are zero. This model must be solved subject to appropriate boundary conditions on the flow (no slip and no penetration at the rigid substrate  $z = 0$ , with a stress balance and a kinematic condition at the free interface  $z = h(x, t)$ ) and anchoring conditions on the director.

### A. Scalings and simplifying assumptions

The full model outlined above is extremely complicated, and we make analytical progress by utilizing certain simplifying assumptions, and by introducing scalings that allow us to justify neglecting terms in the equations that are asymptotically small in the limit that the ratio,  $\delta = H^*/L^*$ , of a characteristic film thickness  $H^*$  to a characteristic lateral lengthscale  $L^*$ , goes to zero. Since we shall now introduce a new set of dimensionless variables, we use a \* superscript henceforth to denote the

dimensional quantities; those without \*’s are now dimensionless. We write

$$(x^*, z^*) = L^*(x, \delta z), \quad (u^*, w^*) = U^*(u, \delta w), \\ t^* = \frac{L^*}{U^*} t, \quad p^* = \frac{\mu^* U^*}{\delta^2 L^*} p,$$

where  $U^*$  is a typical flow velocity in the  $x^*$ -direction (fixed by a balance between gravity and surface tension); and  $\mu^* \equiv \alpha_4/2 > 0$  was chosen as the representative viscosity scaling in the pressure, since this corresponds to the usual viscosity in the isotropic case in (8). All viscosities  $\alpha_i^*$ ,  $\gamma_i^*$  are scaled with  $\mu^*$ , and the dimensionless viscosities that result are assumed to be no larger than order-one. We also write  $h^* = H^*h$  to define the dimensionless drop height.

If  $K^* = K_1^*$  is a representative value of the elastic constants  $K_1^*$ ,  $K_2^*$ ,  $K_3^*$ , (7) gives the appropriate scaling for  $W^*$  as

$$W^* = \frac{K^*}{\delta^2 L^{*2}} W.$$

We now rewrite the governing equations in dimensionless form and assume (as is common in liquid crystals modeling) that  $K_1^* = K_3^* = K^*$ , so that the (dimensionless) elastic energy  $W$  is given by

$$2W = \delta^2 \theta_x^2 + \theta_z^2. \quad (9)$$

The procedure now is to expand all dependent variables asymptotically in powers of  $\delta = H^*/L^*$ , and substitute into Eqs. (1)–(3) to obtain a hierarchy of governing equations at orders 1,  $\delta$ ,  $\delta^2$ , etc.

### B. The governing PDE

In the case that the parameter  $\mathcal{N}_1 = K^*/(\mu^* U^* L^*)$  is order-one (with respect to  $\delta$ ), the coupling term in  $\tilde{\mathbf{g}}$  vanishes to leading order in (1). This equation then reduces to the Euler-Lagrange problem of minimizing  $W$  (subject to appropriate boundary conditions) which, with  $W$  given by (9), is just  $\theta_{zz} = 0$ . Thus,

$$\theta = az + c, \quad (10)$$

where  $a$  and  $c$  are fixed by the boundary conditions on  $\theta$ .

In previous work [4, 5] the cases of strong anchoring (different, constant values of  $\theta$  specified on both surfaces  $z = 0, h$ ) and weak anchoring (a surface energy assigned to each interface, and the Euler-Lagrange minimization carried out explicitly), respectively, were considered. However, neither approach, at least for the accepted Rapini-Papoular choice of surface energy at each interface [3], gives rise to a model that behaves satisfactorily in the vicinity of a contact line. (Both approaches introduce an extra ‘nematic’ term into the standard thin-film equation. In the limit  $h \rightarrow 0$  this extra term in the strong anchoring governing PDE for  $h$  appears as negative diffusion ( $h_{xx}$  on the same side of the PDE as  $h_t$ ) [4];

while in the weak anchoring case the nematic term takes the form  $(h^2 h_x)_x$  [5].) The approach we take here is to propose that the change in director angle,  $ah = \theta_h - \theta_0$  (see (10)), is not fixed, but depends on the film thickness  $h$ . The physical rationale behind this is that, when the film is relatively thick, it is “easy” for the director to adjust to the preferred angles at each interface by bending across the film. However, as the film gets thin, and in particular near contact lines, there is a very large energy penalty to pay for bending between two fixed angles across a very short distance  $h$ . Thus, we introduce an *ad hoc* anchoring condition based on specifying the change in director angle by the formula

$$ah = \theta_h - \theta_0 = \Delta\Theta m(h), \quad (11)$$

where  $\Delta\Theta$  is a constant – the difference between the preferred anchoring angles at the two surfaces – and  $m(h)$  is a monotone increasing function, approaching zero as  $h \rightarrow 0$ , and approaching 1 as  $h \rightarrow \infty$ . This latter condition on  $m$  ensures that the strong anchoring limit (with a fixed director angle jump of  $\Delta\Theta$  across the film) is retrieved for a thick film, while for a vanishingly thin film, the anchoring constraint is relaxed so that there is no mismatch. We emphasize that the basic elastic instability mechanism remains the same; our procedure here amounts to a regularization of the resulting PDE.

It turns out that the choice of  $c$  in Eq. (10) does not affect the subsequent analysis (only the change in director angle is important), so we set  $c = 0$  without loss of generality. With the solution for director angle  $\theta$  now determined as

$$\theta = \frac{\Delta\Theta}{h} m(h) z,$$

the analysis of the momentum equations then proceeds as described in [4, 5]. Provided the reduced Reynolds number based on the representative viscosity  $\mu^* = \alpha_4^*/2$ , given by  $\delta^2 \text{Re} = \delta^2 \rho^* U^* L^* / \mu^*$ , is asymptotically small, and again supposing  $\mathcal{N}_1 = K^* / (\mu^* U^* L^*) = O(1)$ , the governing equations reduce, as is shown in [5], to a single PDE for  $h(x, t)$ :

$$h_t + [(\mathcal{C}h_{xxx} - \mathcal{B}h_x - \mathcal{N}_1 a a_x) \mathcal{I}_1 - \mathcal{N}_1 h a a_x \mathcal{I}_2]_x = 0, \quad (12)$$

where  $\mathcal{C} = \delta^3 \gamma^* / (\mu^* U^*)$  is an inverse capillary number;  $\mathcal{B} = \delta^3 \rho^* g^* L^{*2} / (\mu^* U^*)$  is a Bond number; the quantities  $\mathcal{I}_1, \mathcal{I}_2$  are defined by

$$\mathcal{I}_1 = \frac{F_1(2ah)}{a^3}, \quad \mathcal{I}_2 = \frac{F_2(2ah)}{a^2}, \quad (13)$$

$$F_1(\lambda) = \frac{1}{4} \int_0^\lambda \frac{(\lambda - \xi)^2 d\xi}{\alpha_1 \sin^2 \xi + 2(\eta_b + \eta_c) - 2(\eta_b - \eta_c) \cos \xi}, \quad (14)$$

$$F_2(\lambda) = \frac{1}{2} \int_0^\lambda \frac{(\lambda - \xi) d\xi}{\alpha_1 \sin^2 \xi + 2(\eta_b + \eta_c) - 2(\eta_b - \eta_c) \cos \xi} \quad (15)$$

and the so-called Miesowicz viscosities are given by  $\eta_b = (1 + \alpha_3 + \alpha_6)/2$ ,  $\eta_c = (1 - \alpha_2 + \alpha_5)/2$  (see [7]). Here  $a$  is not defined as in [5] however, but is given by Eq. (11).

Equations (11)–(15) represent a formidable challenge, and progress for the analogous system in [5] was restricted to stability analysis of the flat film solution, together with analysis of some limiting cases (no numerical solutions were computed). Therefore, it is very helpful to simplify the PDE further in order to proceed. One simplification is to approximate the integral expressions (14), (15) by their values in the Newtonian case. Then,  $\alpha_1 = 0$ , while  $\eta_b = \eta_c = 1/2$ , and it may be checked explicitly that  $\mathcal{I}_1 = h^3/3$ ,  $\mathcal{I}_2 = h^2/2$ . Alternatively, one may approximate the integrals in Eqs. (14), (15) by asymptotic expansion in  $\lambda$  as

$$F_1(\lambda) = \frac{\lambda^3}{48\eta_c} + O(\lambda^5), \quad F_2(\lambda) = \frac{\lambda^2}{16\eta_c} + O(\lambda^4), \quad (16)$$

giving  $\mathcal{I}_1 \propto h^3$ ,  $\mathcal{I}_2 \propto h^2$ . While this expansion is strictly valid only for small  $\lambda$  (correspondingly, for small  $h$ ), further justification for this approach can be found in the fact that for large  $h$ , where the asymptotic expansions are not formally valid, the model reduces to the so-called strong anchoring limit studied by Ben Amar & Cummings; the integral expressions (14), (15) can be evaluated analytically, and the same scaling of the corresponding terms with  $h$  is obtained [4]. One can also (for  $m(h)$  as given in (18) below or a qualitatively similar form) plot the full integral expressions (14), (15) as functions of  $\lambda$  and, to a good approximation, fit a multiple of  $h^3$  and a multiple of  $h^2$  respectively, though we omit such plots for brevity in this paper. Taking only the leading terms in the expansions (16) ultimately yields the same result (after a rescaling of time) as the Newtonian approximation. Therefore we substitute the Newtonian approximation in Eq. (12), which leads to

$$h_t + \left[ \frac{h^3}{3} (\mathcal{C}h_{xxx} - \mathcal{B}h_x) + \frac{5\mathcal{N}_1}{6} (\Delta\Theta)^2 (m^2 - h m m') h_x \right]_x = 0,$$

or, rescaling time to eliminate the factor of 1/3 for convenience,

$$h_t + [h^3 (\mathcal{C}h_{xxx} - \mathcal{B}h_x) + \mathcal{N} (m^2 - h m m') h_x]_x = 0, \quad (17)$$

where  $\mathcal{N} = 5\mathcal{N}_1 (\Delta\Theta)^2 / 2 = 5(\Delta\Theta)^2 K^* / (2\mu^* U^* L^*)$ .

There are many possible forms we could choose for  $m(h)$  that satisfy our basic requirements; we take

$$m(h) = \frac{h^{3/2}}{\beta^{3/2} + h^{3/2}}, \quad (18)$$

where  $\beta = \beta^* / H^*$ ,  $\beta^*$  being a lengthscale over which the anchoring condition is relaxed. For a film of height  $h^* \ll \beta^*$  anchoring is weak, and for  $h^* \gg \beta^*$  it is strong (note that in the limit  $\beta \rightarrow 0$  we indeed recover the strong anchoring model of [4], the destabilizing nematic term in  $\mathcal{N}$  in Eq. (17) taking the form of negative diffusion). In addition to satisfying the conditions  $m \rightarrow 0$  as  $h \rightarrow 0$ ,  $m \rightarrow 1$  as  $h \rightarrow \infty$ , the functional form (18) has the feature that as  $h \rightarrow 0$ , the nematic term in the governing

thin film equation reduces to the same form as the gravity term. As  $h \rightarrow 0$ , the asymptotic form of Eq. (17) is

$$\frac{\partial h}{\partial t} + \frac{\partial}{\partial x} \left[ Ch^3 h_{xxx} - \left( \mathcal{B} + \frac{\mathcal{N}}{2\beta^3} \right) h^3 h_x \right] = 0, \quad (19)$$

so the model admits solutions that are regular at a contact line (or apparent contact line); such drops would simply be expected to spread faster than the Newtonian equivalents. This is consistent with the experimental observations [1], which do indeed note faster spreading rates for the nematic drops than are seen in the equivalent Newtonian case (this issue is discussed further in §III D). We note that choices other than (18) for the function  $m(h)$  were considered, in particular, different exponents of  $h$ . Exponents less than  $3/2$  lead to non-spreading droplets, while exponents greater than  $3/2$  lead to droplets that spread at the same rate as Newtonian ones. Only the choice  $3/2$  gives the augmented spreading speed in line with the experimental data.

### III. ANALYSIS AND RESULTS

Our final model consists of the PDE (17), with  $m(h)$  given by (18). We have four dimensionless parameters: the inverse capillary number  $\mathcal{C}$ , the Bond number  $\mathcal{B}$ , the inverse Ericksen number  $\mathcal{N}$ , and the phenomenological dimensionless adjustment length  $\beta$ , which measures the film height over which anchoring adjusts from strong to weak.

We first discuss appropriate values of the dimensionless parameters, before carrying out a linear stability analysis of simple cases, which gives us insight into the general characteristics of this model. We then present numerical simulations of 2D “drops”, illustrating the variety of behaviors that the model can exhibit. We interpret our results in the light of the linear stability analysis and the experimental data of Poulard & Cazabat [1].

#### A. Dimensionless parameter values

With four dimensionless parameters (and an initial condition) the solution space for the PDE (17) is potentially very large. In all of our simulations we assume a balance between surface tension and gravity, setting  $\mathcal{C} = \mathcal{B} = 1$ , and investigate the effect of the parameters  $\mathcal{N}$  and  $\beta$ , representing (respectively) the relative importance of elasticity to viscosity, and the “anchoring relaxation lengthscale”.

With our assumptions of unit capillary and Bond numbers, the horizontal velocity and lengthscales are  $U^* = \delta^3 \rho^* g^* L^{*2} / \mu^*$ ,  $L^* = \sqrt{\gamma^* / (\rho^* g^*)}$ . The parameter  $\mathcal{N} \equiv 2(\Delta\Theta)^2 K^* / (\mu^* U^* L^*)$  then becomes  $\mathcal{N} = 2(\Delta\Theta)^2 K^* / (\rho^* g^* H^{*3})$  ( $H^* = \delta L^*$  is a typical droplet height, or film thickness). Hence, if we choose a representative value of  $H^*$  that we assume is appropriate

for all the experiments (equivalent to choosing a droplet aspect ratio  $\delta$ ), and a value for  $\Delta\Theta$ , we fix  $\mathcal{N}$ .

For a given nematic-substrate system, the parameter  $\beta = \beta^* / H^*$  may be expected to depend on the humidity in the experiments, which was varied significantly. Recall that the change in director angle,  $\theta_h - \theta_0$ , across the film, depends on  $\beta$  via the relation  $\theta_h - \theta_0 = \Delta\Theta m(h) = \Delta\Theta h^{3/2} / (h^{3/2} + \beta^{3/2})$ . While we have no *a priori* evidence for the size of  $\beta^*$ , if we identify it as the lengthscale on which the smaller of the two nematic surface energies (that at the liquid crystal–air interface, and that at the liquid crystal–substrate interface),  $A^*$  say, and internal elasticity balance, then we have

$$\frac{K^*(\Delta\Theta)^2}{\beta^{*2}} \sim \frac{A^*}{\beta^*} \quad \Rightarrow \quad \beta^* = \frac{K^*(\Delta\Theta)^2}{A^*}.$$

Experimental measurements exist for  $A^*$  for various nematics, thus we can estimate  $\beta^*$ . With  $K^* \sim 10^{-11}$  N [9],  $A^* \sim 10^{-5}$ – $10^{-4}$  Nm<sup>-1</sup> [10–12], and  $\Delta\Theta = O(1)$  [1], we obtain estimates in the range  $\beta^* \in (0.1, 1)$   $\mu$ m. We note however that the representative surface energy  $A^*$  may well depend on relative humidity, as may the angle  $\Delta\Theta$  (the latter is suggested by the experiments of [13], where it is shown that an anchoring transition, at which the anchoring angle changes fairly abruptly as humidity is varied, can occur at high humidity). Regarding a representative value of droplet height  $H^*$ , the information provided in Fig. 3 of [1] suggests that a typical value is on the order of few  $\mu$ m; using  $H^* \sim 1$ – $10$   $\mu$ m then gives  $\beta \in (10^{-2}, 1)$ .

For the value of  $\mathcal{N}$ , if we take  $H^* = 10$   $\mu$ m, and use  $K^* = 10^{-11}$  N [9] as a representative value then

$$\mathcal{N} = \frac{2(\Delta\Theta)^2 K^*}{\rho^* g^* H^{*3}} \sim \frac{2(\Delta\Theta)^2 \cdot 10^{-11}}{10^3 \cdot 10 \cdot 10^{-15}} = 2(\Delta\Theta)^2. \quad (20)$$

Using a representative thickness  $H^* = 1$   $\mu$ m however gives a value for  $\mathcal{N}$  that is  $10^3$  times larger. Hence, we may suppose that  $\mathcal{N}$  lies somewhere in the range  $(1, 1 \times 10^3) \times (\Delta\Theta)^2$ , for the experiments of [1]. If the preferred anchoring is planar at the substrate and homeotropic at the free surface ([1], Introduction, paragraph 3), then  $(\Delta\Theta)^2 = \pi^2/4$ , giving  $\mathcal{N}$  somewhere in the range  $(5, 5 \times 10^3)$ . As noted above however,  $\Delta\Theta$  can vary with relative humidity [13].

With  $\mathcal{B} = \mathcal{C} = 1$ , droplets of variable size can be considered in the model by means of the dimensionless initial condition (represented by some  $h_0$ ). In line with the above discussion, we expect parameters  $\beta$  and  $\mathcal{N}$  to vary with the relative humidity, giving a 3-parameter system to study.

#### B. Linear stability analysis: the flat film

Linear stability analysis of the governing PDE (17) is complicated by the fact that exact solutions are hard to find explicitly. We focus attention on the simplest

exact solutions: flat films  $h = h_0$ . Writing  $h(x, t) = h_0 + \epsilon h_1(x, t) + \dots$ , where  $0 < \epsilon \ll 1$  is a small parameter, and substituting in (17) (with  $\mathcal{B} = \mathcal{C} = 1$ ), at  $O(\epsilon)$  we find

$$h_{1t} + h_0^3 h_{1xxxx} - h_0^3 \left( 1 - \mathcal{N} \frac{(h_0^{3/2} - \beta^{3/2}/2)}{(h_0^{3/2} + \beta^{3/2})^3} \right) h_{1xx} = 0.$$

Assuming solutions of the form  $h_1 = h_{10} e^{ikx - \omega t}$ , we obtain the dispersion relation

$$\omega = -h_0^3 k^2 \left( k^2 + \left( 1 - \mathcal{N} \frac{(h_0^{3/2} - \beta^{3/2}/2)}{(h_0^{3/2} + \beta^{3/2})^3} \right) \right).$$

Writing  $M(h_0) = (h_0^{3/2} - \beta^{3/2}/2)/(h_0^{3/2} + \beta^{3/2})^3$ , we then have instability of the flat film to sufficiently long-wavelength perturbations if  $\mathcal{N}M(h_0) > 1$ . When this is the case, perturbations with wavenumbers  $k \in (0, k_c)$  are unstable, where  $k_c = \sqrt{\mathcal{N}M(h_0) - 1}$ ; and the fastest-growing wavenumber is  $k_m = \sqrt{(\mathcal{N}M(h_0) - 1)/2}$ , with wavelength

$$\lambda_m = \frac{2\pi}{k_m} = \frac{2\pi}{\sqrt{(\mathcal{N}M(h_0) - 1)/2}} \quad (21)$$

and growth-rate  $\omega_m = h_0^3(\mathcal{N}M(h_0) - 1)^2/4$ . Figures 3, 4, and 5 show three two-dimensional slices of the stability diagram in  $(\beta, h_0, \mathcal{N})$  space, together with the particular parameter values for which drop evolution is discussed below. We see that the instability region increases significantly for larger values of  $\mathcal{N}$ , or smaller values of  $\beta$ . However, there exists a range of film thicknesses for which a flat film is stable.

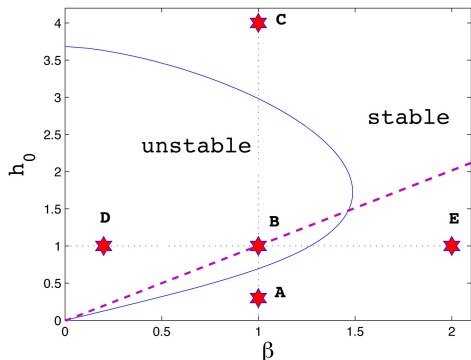


FIG. 3: Stability diagram in  $(\beta, h_0)$ -space for  $\mathcal{N} = 50$ . The region enclosed by the solid curve represents unstable solutions. The dashed line is  $h_0 = \beta$ ; roughly speaking, when we extrapolate our flat film analysis to the droplet scenario, experiments lying below this line will spread, while those above it will not, as discussed in the text. A: ( $\beta = 1, h_0 = 0.3, \mathcal{N} = 50$ ). B: ( $\beta = 1, h_0 = 1, \mathcal{N} = 50$ ). C: ( $\beta = 1, h_0 = 4, \mathcal{N} = 50$ ). D: ( $\beta = 0.2, h_0 = 1, \mathcal{N} = 50$ ). E: ( $\beta = 2, h_0 = 1, \mathcal{N} = 50$ ).

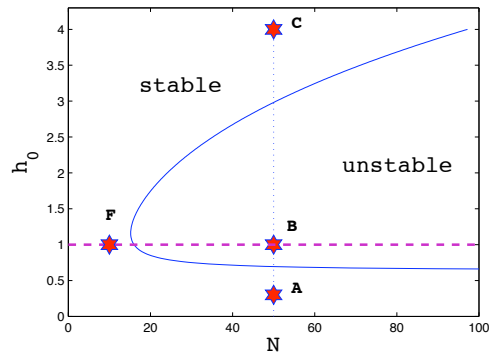


FIG. 4: Stability diagrams in  $(\mathcal{N}, h_0)$ -space for  $\beta = 1$ . The region enclosed by the solid curve represents unstable solutions, the dashed line is  $h_0 = \beta$ . A: ( $\beta = 1, h_0 = 0.3, \mathcal{N} = 50$ ). B: ( $\beta = 1, h_0 = 1, \mathcal{N} = 50$ ). C: ( $\beta = 1, h_0 = 4, \mathcal{N} = 50$ ). F: ( $\beta = 1, h_0 = 1, \mathcal{N} = 10$ ).

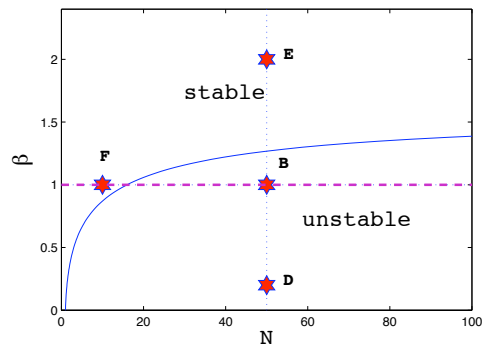


FIG. 5: Stability diagram in  $(\mathcal{N}, \beta)$ -space for  $h_0 = 1$ . The region enclosed by the solid curve represents unstable solutions. The dashed line is  $h_0 = \beta$ . B: ( $\beta = 1, h_0 = 1, \mathcal{N} = 50$ ). D: ( $\beta = 0.2, h_0 = 1, \mathcal{N} = 50$ ). E: ( $\beta = 2, h_0 = 1, \mathcal{N} = 50$ ). F: ( $\beta = 1, h_0 = 1, \mathcal{N} = 10$ ).

### C. Extrapolation to the case of spreading droplets

Although our stability analysis is valid only for a flat film, and thus is not strictly applicable to a spreading drop of the kind in the experiments, we expect to be able to extract qualitative predictions for spreading drop simulations. Our numerical experiments bear out this expectation: for all simulations we have carried out (including many more than are shown here) we find that flat film linear stability analysis is an excellent indicator of stability properties of the droplets considered. For a spreading droplet there is of course no precise definition of  $h_0$ , the film height in the linear stability analysis, but in all our simulations we consider a 2D droplet whose initial shape is close to a rectangle (though with smoothed corners), of width 10 and height  $h_0$ .

To illustrate the drop evolution for different values of the parameters we refer to our stability diagrams, Figs. 3, 4, and 5, each of which fixes a representative value of a given parameter. For each such fixed parameter value we carry out simulations showing drop evolution for typical values of the other two parameters. These points are marked by stars, and a capital letter for later reference. For example, Figs. 6, 7 and 8 show the case for which  $\beta$  and  $\mathcal{N}$  are fixed while film height  $h_0$  is varied (corresponding to points A, B, C in Fig. 3 or 4), while Figs. 7, 9 and 10 show the effect of varying  $\beta$  with parameters  $\mathcal{N}$  and  $h_0$  being fixed (corresponding to points B, D, E in Figs. 3 or 5). The initial condition is shown as a dashed curve in each case.

Numerical simulations are performed using a finite-difference method. We have implemented an implicit 2nd-order Crank-Nicolson method in time, 2nd-order discretization in space and Newton's method to solve the nonlinear system at each time step. For numerical convenience a thin prewetted layer of thickness  $b = 0.01$  is included in all simulations, as is commonly done for models of this kind (see, e.g., [14]); this is particularly appropriate here due to the complete wetting conditions of the experiments. We have verified that the evolution on scales larger than the prewetted layer thickness  $b$  is independent of the exact value given to this quantity, as long as it is small compared with  $h_0$ . At the domain boundaries we impose  $h = b$  and  $h_x = 0$ .

As a general observation, we note that when  $h \gg \beta$  in the ‘‘anchoring’’ function  $m(h)$  (see Eq. (18)) then we have effectively a strong anchoring condition. This behaves as a negative diffusion term in Eq. (17), and hence does not permit spreading. However when  $h \ll \beta$  anchoring is relaxed and there is no barrier to spreading (the film is essentially Newtonian where its height is much smaller than  $\beta$ , as Eq. (19) shows). We therefore expect an approximate transition from spreading to non-spreading behavior according to whether or not  $h_0$  is much less than or greater than  $\beta$ . For this reason, we indicate  $h_0 = \beta$  on Figs. 3, 4, and 5 as a dashed line.

In Fig. 6 we see perhaps the simplest case of a stable spreading drop, with behavior similar to the Newtonian case. This corresponds to point A in the stability diagrams 3 and 4, which lies in the region of stability. Fig. 7 shows the evolution when  $h_0$  is increased to fall into the unstable region; point B in the stability diagrams. In the early stages of evolution, the initial single drop evolves into a drop with two humps (Fig. 7(a)). As the drop spreads, the two humps merge into one (Fig. 7(b)), which eventually disappears (Fig. 7(c)).

We note in passing the interesting similarity of the instability pattern and the spreading behavior in Fig. 7 to the experimental results for spreading nano-scale drops, Fig. 2. Although our model is not expected to apply to such tiny droplets, the experiments of [2] were carried out in complete wetting conditions, and intermolecular forces (not included in our model) may not be a dominant effect.

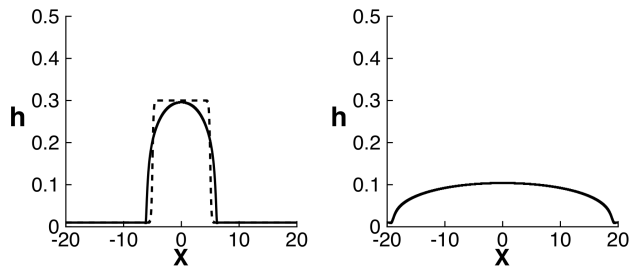


FIG. 6: Evolution of a spreading drop for parameters corresponding to point A in stability diagrams 3 and 4:  $h_0 = 0.3$ ,  $\beta = 1$ ,  $\mathcal{N} = 50$ . The figure in LHS shows  $t = 0$  (dashed) and  $t = 10$ . The figure in the RHS shows  $t = 4000$ .

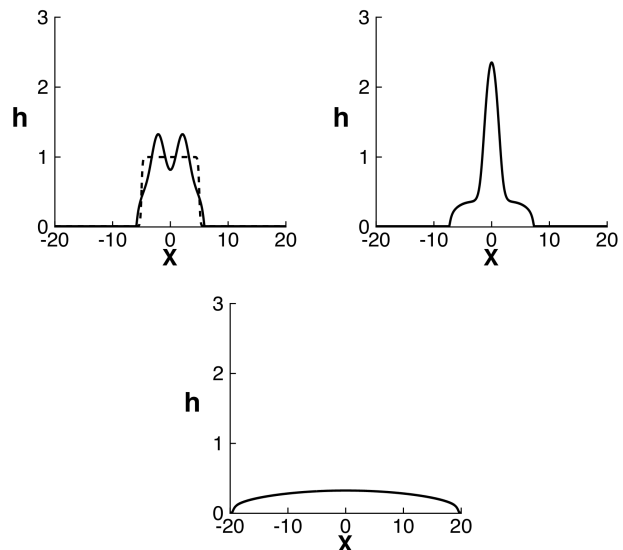


FIG. 7: Evolution of a drop for parameters corresponding to point B in stability diagrams 3, 4, and 5:  $h_0 = 1$ ,  $\beta = 1$ ,  $\mathcal{N} = 50$ . The figure in upper left shows  $t = 0$  (dashed) and  $t = 1$ . The figure in the upper right shows  $t = 10$ . The figure in lower center shows  $t = 400$ .

As the initial drop thickness  $h_0$  is further increased, we again move into the stable region (point C on the stability diagrams) and no instability is observed in the drop evolution, as shown in Fig. 8. In addition, there appears to be a well-defined thickness, such that the portion of the drop below this thickness spreads, while the upper part of the drop essentially stands still. This ties in with the observation above that where  $h_0 \gg \beta$ , spreading does not occur.

Figure 9 shows the drop evolution for small  $\beta$ , corresponding to point D in the stability diagrams. The flat film  $h_0 = 1$  is unstable in this case, which leads to the appearance of several humps (Fig. 9(a)). The humps evolve into drops and stop spreading after a certain time (Fig. 9(b)).

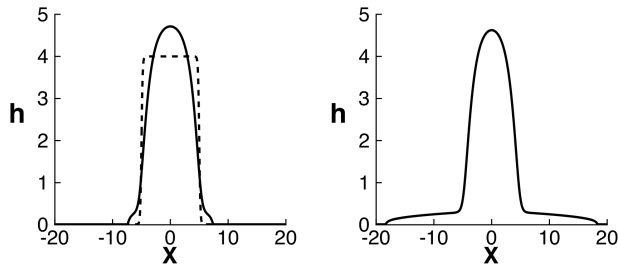


FIG. 8: Evolution of a drop for parameters corresponding to point C in stability diagrams 3 and 4:  $h_0 = 4$ ,  $\beta = 1$ ,  $\mathcal{N} = 50$ . The figure in LHS shows  $t = 0$  (dashed) and  $t = 10$ . The figure in the RHS shows  $t = 500$ .

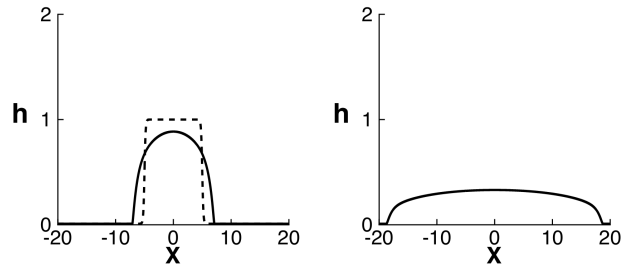


FIG. 10: Evolution of a drop for parameters corresponding to point E in stability diagrams 3 and 5:  $h_0 = 1$ ,  $\beta = 2$ ,  $\mathcal{N} = 50$ . The figure in LHS shows  $t = 0$  (dashed) and  $t = 10$ . The figure in the RHS shows  $t = 1000$ .

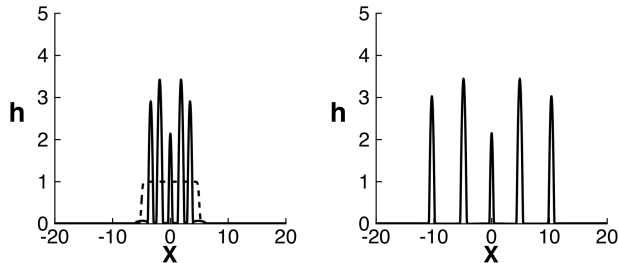


FIG. 9: Evolution of a drop for parameters corresponding to point D in stability diagrams 3 and 5:  $h_0 = 1$ ,  $\beta = 0.2$ ,  $\mathcal{N} = 50$ . The figure in LHS shows  $t = 0$  (dashed) and  $t = 10$ . The figure in the RHS shows  $t = 1000$ .

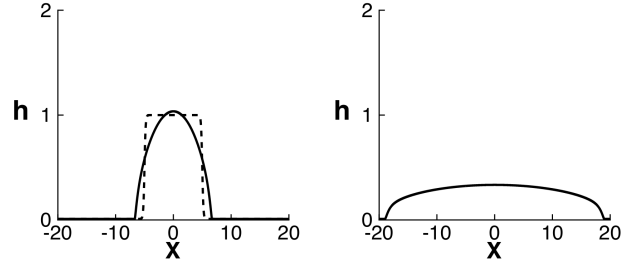


FIG. 11: Evolution of a drop for parameters corresponding to point F in stability diagrams 4 and 5:  $h_0 = 1$ ,  $\beta = 1$ ,  $\mathcal{N} = 10$ . The figure in LHS shows  $t = 0$  (dashed) and  $t = 10$ . The figure in the RHS shows  $t = 1000$ .

We note that in general there are two consequences of varying  $\beta$ : the stability of the drop, and its ability to spread may both change. As  $\beta$  is increased from 0.2 to 1 (moving from point D to B on the stability diagrams), the most unstable wavelength increases and the number of humps decreases for a given size of drop (vis. Fig. 7(a) and Fig. 9(a)). The other important feature is that humps move apart for the non-spreading case, while they merge into one single hump for the spreading one (vis. Fig. 7(b) and Fig. 9(b)). Figure 10 shows the results for yet larger  $\beta$  (point E on the stability diagrams). This point lies back in the stable region and no humps are observed. In summary, as we vary the value of  $\beta$  from low to high in these simulations we change the behavior, from an unstable non-spreading drop, to an unstable spreading drop, and finally to a stable spreading drop.

Figures 7 and 11 show the effect of varying  $\mathcal{N}$ . As expected from the stability diagram, increasing  $\mathcal{N}$  makes the drop unstable. The other interesting feature is that the unstable drop spreads faster than the stable one (compare the times of Fig. 7(c) and Fig. 11(b)). This phenomenon is consistent with the  $h \rightarrow 0$  analysis of Eq. (19), which suggested that the spreading speed should be faster as  $\mathcal{N}$  is increased, and is discussed further below.

#### D. Spreading rates

Given the experimental observation that the nematic droplets appear to spread faster than the Newtonian equivalents, it is of interest to look at the large-time behavior of spreading drops and see what trends can be extracted. Since only certain regions of parameter space correspond to well-defined, stable, spreading droplets (namely, within the stability region in Figs. 3, 4, 5 and with  $h_0 < \beta$ , as discussed in §III C), we restrict attention to such droplets.

Figure 12 shows the effective contact line position and maximum droplet height, as functions of time, on a log-log plot, for the droplet simulations of Figs. 6, 10 and 11 (corresponding to points A, E and F respectively in the stability diagrams 3, 4, 5). (Effective contact line position is defined as the inflection point of the drop profile  $h(x, t)$ .) The Newtonian results appear to approach a straightforward power-law with exponents  $\pm 0.2$  for the contact line position and droplet height, respectively (confirming conservation of mass for these droplets). This is in agreement with the scalings in the similarity solutions for viscous gravity currents presented by Huppert [15] (no surface tension; flow is governed by the so-called porous medium equation). Since at large

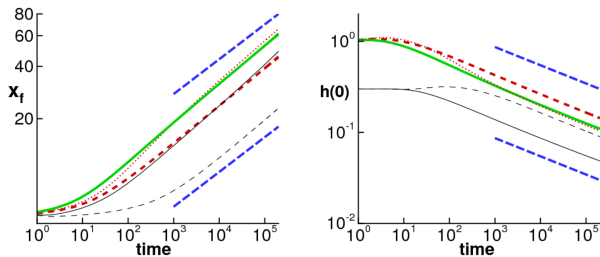


FIG. 12: (LHS) Effective contact line position  $x_f$  and (RHS) maximum droplet height  $h(0, t)$  as a function of time, for the droplets of fig. 6 ( $h_0 = 0.3$ ,  $\mathcal{N} = 50$ ,  $\beta = 1$ ; thin black solid), fig. 10 ( $h_0 = 1$ ,  $\mathcal{N} = 50$ ,  $\beta = 2$ ; thick solid, green online), and fig. 11 ( $h_0 = 1$ ,  $\mathcal{N} = 10$ ,  $\beta = 1$ ; thin dotted, red online). Also shown are the two corresponding Newtonian results ( $\mathcal{N} = 0$ ): for initial conditions  $h_0 = 0.3$  (thin black dashed), and  $h_0 = 1$  (thick dashed, red online). A power-law with exponent  $\pm 0.2$  is indicated by the thick dashes (blue online).

times gravity dominates in the Newtonian version of our problem, this is to be expected. This 2D result may be contrasted with radial spreading of 3D Newtonian droplets, where exponents 0.125,  $-0.25$  are extracted for the contact line position and maximum droplet height at large times, respectively [15]. Slight upward curvature for long times (visible perhaps most clearly for the Newtonian case with  $h_0 = 0.3$  in Fig. 12(a)) is a consequence of the presence of the precursor, as discussed in some detail in [16]. The behavior of the nematic droplets is more complicated, as we would expect given the nonlinear dependence of the anchoring function  $m(h)$  on  $h$ . At large times the behavior is close to the power-law of the corresponding 2D Newtonian case but in all cases the (apparent) multiplicative prefactor in the supposed power-law is larger for the nematic droplet than the Newtonian equivalent. Since we study only 2D droplets in this paper a quantitative comparison with experiments is not possible, but we note that these observations are in line with the general trend observed, that nematic droplets appear to spread faster than their Newtonian counterparts.

### E. Implications for the experiments

The two trends observed by Poulard & Cazabat are that higher humidity correlates with droplet instability, as does larger droplet size. They also state (§IV.1) that at low RH the drops do not spread macroscopically. These observations are only qualitative however, and likely the interplay between the individual effects of droplet size and humidity is complex. We note in addition that although humidity can affect surface tension (so that in principle the capillary number could change), we focus here on its effect on  $\beta$  and  $\mathcal{N}$ . We deal with each of these in turn.

If  $\mathcal{N}$  is fixed then we hypothesize that  $\beta$  is a decreasing

function of humidity: that is, larger values of  $\beta$  correspond to low humidity, and vice versa. This correlation would suggest that at low humidity anchoring is weaker (for a given droplet height  $h$ , the value of  $m(h)$  decreases as  $\beta$  increases), and that effective anchoring strength increases with humidity. If this is so then our model supports this qualitative trend, since in general large values of  $\beta$  give rise numerically to stable drops, while small values of  $\beta$  (for droplet height  $h$  lying in the appropriate range) give rise to unstable drops. We note also that under this assumption our model suggests additional predictions, which would be interesting to test with future experiments: firstly, sufficiently large droplets ( $h_0$  above the upper branch of the stability curve in Fig. 3) should again become stable; and secondly, at sufficiently low humidity (sufficiently large  $\beta$ ) droplets of any size should be stable.

Suppose now that  $\beta$  is fixed, while  $\mathcal{N}$  varies with humidity, via its dependence on  $\Delta\Theta$ . Humidity is known to affect anchoring angles; the work of [13] suggests that  $\Delta\Theta$ , and hence  $\mathcal{N}$ , could be an increasing function of humidity. Looking at the fixed- $\beta$  stability diagram, Fig. 4, the general trend for increasing humidity is then correct, since the region of instability increases in size as  $\mathcal{N}$  increases.

Temperature is also investigated experimentally. This quantity can, of course, influence many variables, but Poulard & Cazabat focus chiefly on its effect on the elastic constant  $K^*$ , which decreases as temperature increases [18]. While the dependence on temperature is not precisely documented, the observed trend is that increasing temperature suppresses the instabilities. This general effect is captured by the model, since as  $K^*$  decreases,  $\mathcal{N}$  decreases, and the region of instability shrinks (Figs. 4 and 5). The data shown in Fig. 4 of [9] show that the variation of  $K^*$  can be quite profound over only a few degrees Kelvin, so that the size of the stability region can shrink (or grow) appreciably as temperature is varied.

### Wavelength of the instability

The linear stability analysis gives us a maximal growth-rate  $\omega_m$ , and a corresponding wavelength  $\lambda_m$  (Eq. (21)), which is the wavelength we would expect to dominate in the early stages of the instability. While the analysis is valid only for a flat film, we hypothesize that it should give us a qualitative estimate of the wavelength observed in the spreading droplet experiments of [1]. Since there are two distinct wavelengths observed, there are two candidates for our model to explain.

The photographs in Fig. 1 suggest rough values for the two wavelengths  $\lambda_{1m}^* \approx 5 \mu\text{m}$ ,  $\lambda_{2m}^* \approx 500 \mu\text{m}$  (we estimate values from Figs. 1 (c) and (e), where each of the instabilities appears independently so the two are not interacting). Our model predicts  $\lambda_m = \lambda_m^*/L^*$ , so before fitting we need to estimate  $L^*$  for the system. Our balance of capillary and gravity forces specifies  $L^*$  as the

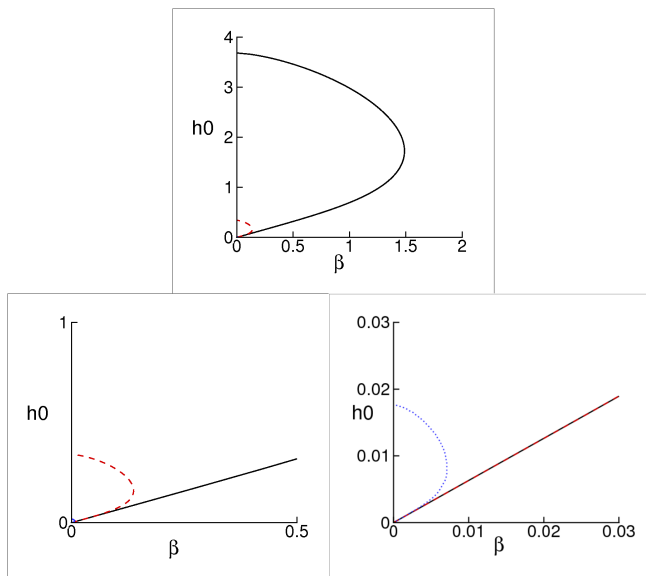


FIG. 13: Stability diagrams in  $(\beta, h_0)$ -space for  $\mathcal{N} = 50$ , showing where the curves (22) (a) and (b) lie within it. The top and bottom LHS figures show the stability region boundary (solid), and the curve (22)(a) on which the experiment of Fig. 1(e) should lie (dashed, zoomed in bottom LHS figure). The bottom RHS figure, also zoomed, shows the stability region boundary (solid), and the curve (22)(b) on which the experiment of Fig. 1(c) should lie (dotted).

capillary length,  $L^* = \sqrt{\gamma^*/(\rho^*g^*)}$ , and Tarakhan [17] gives the interfacial tension of 5CB over a reasonable range of temperatures as  $\gamma^* \approx 3.5 \times 10^{-2} \text{ Nm}^{-1}$ . With  $\rho^* = 10^3 \text{ kg m}^{-3}$ , this fixes  $L^* \approx 1.9 \text{ mm}$ . Then, we find  $\lambda_{1m} = \lambda_{1m}^*/L^* \approx 2.5 \times 10^{-3}$ , and  $\lambda_{2m} = \lambda_{2m}^*/L^* \approx 0.25$ . Using the prediction (21) for  $\lambda_m$ , we find that

$$\mathcal{N}M(h_0) \approx \left( \frac{2\pi\sqrt{2}}{\lambda_m} \right)^2 \approx \begin{cases} 128\pi^2 & \text{long (a)} \\ \frac{32\pi^2}{25} \times 10^6 & \text{short (b)} \end{cases} \quad (22)$$

where, recall,  $M(h_0) = (h_0^{3/2} - \beta^{3/2}/2)/(h_0^{3/2} + \beta^{3/2})^3$ . For a given value of  $\mathcal{N}$  we can plot the curves represented by (22); if the model is valid then the experimental results should lie somewhere on one of these curves. Note that we cannot expect our model, as presented, to account for the presence of two distinct instabilities. Figure 13 shows the curves (22) for  $\mathcal{N} = 50$ . For this case, the vertical lengthscale is  $H^* = 5.8 \mu\text{m}$  (from the  $\mathcal{N}$ -value; see (20)). The dashed curves in Fig. 13 then give upper limits on the values of  $h_0$  for the small and large instabilities, which, with  $H^* = 5.8 \mu\text{m}$ , yield the dimensional droplet height estimates  $h_0^* \lesssim 8 \times 10^{-8} \text{ m}$  for the small instability, and  $h_0^* \lesssim 1.9 \times 10^{-6} \text{ m}$  for the long instability. Hence, unless we hypothesize that the small instability originates very near the contact line, where the droplet height is very small indeed, it seems unlikely that our model explains this instability. The droplet height associated with the long wavelength instability seems much more reasonable,

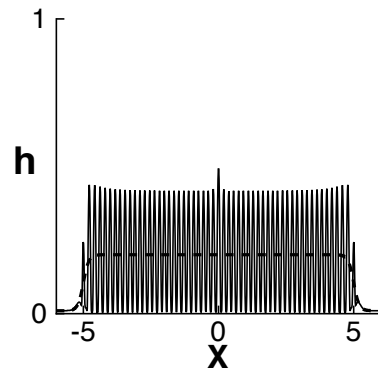


FIG. 14: Simulation of an unstable drop, consistent with our estimate of where in parameter space the experiment of Fig. 1(e) should lie. Parameters are:  $h_0 = 0.2$ ,  $\beta = 0.1$ ,  $\mathcal{N} = 50$ , and the drop is shown at times  $t = 0$  (dashed) and  $t = 0.01$ .

given what we know of the experiments. Although in the experimental photos reproduced here the larger instability is associated with large-scale defects (visible in the photos as lines), these defects appear not to be present when the instability originates, but rather seem to be caused by the instability (see the time-lapse photograph in Fig. 6 of [1]). We note in passing that our conclusions above are not affected by the particular value we assume for  $\mathcal{N}$ .

Figure 14 shows a simulation of our model for parameter values consistent with the long instability (22)(a):  $h_0 = 0.2$ ,  $\beta = 0.1$ ,  $\mathcal{N} = 50$ . Clearly the results are in the (highly) unstable regime; and we note that the dimensionless instability wavelength that dominates is  $\lambda_{2m} \approx 0.25$ , in agreement with our estimates above.

#### IV. DISCUSSION & CONCLUSIONS

We have presented a new model for spreading of a thin film of nematic liquid crystal, in which the traditional anchoring boundary conditions on the director (either strong anchoring, or weak ‘‘Rapini-Papoular’’ anchoring, neither of which are suitable to describe a very thin spreading film) are replaced by a new condition that allows anchoring strength to relax as the film height goes to zero. Simple linear stability analysis for a flat film appears to serve as a very good indicator of the behavior of more complicated spreading drops, even providing reasonable estimates of the wavelength of droplet instabilities well into the nonlinear regime. The basic mechanism driving the instability is the mismatch in anchoring angles at the rigid substrate and the drop’s free surface. This mismatch means that the director has to bend across the film, and for sufficiently thin films, this requires a large energy penalty, which is destabilizing.

While we are still some way from simulations of 3D

spreading drops that can reproduce the experimental results of Poulard & Cazabat [1], we nonetheless believe that this model is a good starting-point for a description of spreading nematic droplets. In particular, we suggest that our model can account (at least qualitatively) for the longer wavelength instability seen in these experiments.

In addition, the fact that some of our simulation results – e.g., Fig. 7 – appear visually very similar to the unstable behavior of spreading nano-scale drops as seen in the experiments of Bénichou *et al.* (see Fig. 2, from [2]) suggests the possibility that similar modeling could be profitably applied here also. In principle, since wetting is complete in the experiments of [2] (and thus the effect of intermolecular forces such as van der Waals’ are likely negligible even in this nanoscale regime), our model in its most general form may well be applicable. (We note in this context that the relevant lengthscale, specified in our model by the dimensional version of the parameter  $\beta$ , which allows the switch between strong and weak anchoring, can easily vary by orders of magnitude for different liquid crystal materials and substrates.) However, the representative scalings chosen in our paper (in particular, our assumptions of unit capillary and Bond numbers) are certainly not applicable to such tiny droplets and, since our stability analysis is restricted to the particular choice of scalings made, our conclusions about when and how stability will be manifested would not, of course, extend to these experiments. Nonetheless, the similarities observed between these nanoscale observations and some of

our simulations are intriguing, and suggestive of a need for a further modeling study on smaller scales.

As mentioned already, while our model accounts for the internal elasticity associated with the nematic liquid crystal molecules, it is implicitly assumed that the director field varies slowly in the plane of the spreading droplet, so that our model cannot describe any situation in which defects in the director (such as are certainly observed in the experiments) are present. Thus if our model does indeed provide the correct mechanism for the observed instabilities, then the presence of the defects could be incidental. We note in this respect that although Figs. 1(d) and (e) certainly exhibit defects, examination of a time-lapse photograph shown in [1] (Fig. 6 in that paper) suggests that the defects may appear after the instability has been initiated. However, we view the inability to describe defects as a shortcoming of our model, and intend to rectify this in future work.

### Acknowledgements

This work was supported by the NSF under grant DMS-0908158. The authors would like to acknowledge informative and useful discussions with A.M. Cazabat and M. Ben Amar. We also thank A.M. Cazabat for permission to use the experimental photos.

- 
- [1] Poulard, C., Cazabat, A.M. Spontaneous spreading of nematic liquid crystals. *Langmuir* **21**, 6270-6276 (2005).
- [2] Bénichou, O., Cachile, M., Cazabat, A.M., Poulard, C., Valignat, M.P., Vandenbrouck, F., Van Effenterre, D. Thin films in wetting and spreading. *Adv. Coll. Int. Sci.* **100-102**, 381-398 (2003).
- [3] Rapini, A. & Papoular, M. *J. Phys. (Paris) Colloq.* **30**, C4, 54 (1969).
- [4] Ben Amar, M., Cummings, L.J. Fingering instabilities in driven thin nematic films. *Phys. Fluids* **13**, 1160-1166 (2001).
- [5] Cummings, L.J. Evolution of a thin film of nematic liquid crystal with anisotropic surface energy. *Europ. J. Appl. Math.* **15** (6), 651-677 (2004).
- [6] Chandrasekhar, S. *Liquid Crystals* (2nd Ed.), Cambridge University Press, Cambridge (1992).
- [7] DeGennes, P.G., Prost, J. *The Physics of Liquid Crystals* (2nd Ed.) International Series of Monographs on Physics (83), Oxford Science Publications, Oxford (1993).
- [8] Leslie, F.M. Theory of flow phenomena in liquid crystals. *Adv. Liquid Crystals* **4**, 1-81 (1979).
- [9] DasGupta, S., Roy, S.K. Splay and bend elastic constants and rotational viscosity coefficient in a mixture of 4-4'-n-pentyl-cyanobiphenyl and 4-4'-n-decyl-cyanobiphenyl. *Phys. Lett. A* **306**, 235-242 (2003).
- [10] Mada, H., & Sato, S. Pretilt angle dependence of azimuthal anchoring energy in nematic liquid crystals. *Jpn. J. Appl. Phys.* **38**, L1118-L1120 (1999).
- [11] O’Neill, M., Kelly, S.M. Photoinduced surface alignment for liquid crystal displays. *J. Phys. D: Appl. Phys.* **33**, R67-R84 (2000).
- [12] Okubo, K., Kimura, M., Akahane, T. Measurement of genuine azimuthal anchoring energy in consideration of liquid crystal molecular adsorption on alignment film. *Jpn. J. Appl. Phys.* **42**, 6428-6433 (2003).
- [13] Bechhoefer, J., Jerome, B., Pieranski, P. Systematic studies of the anchoring transition in nematic liquid crystals. *Phys. Rev. A*, **41** (6), 3187-3192 (1990).
- [14] Diez, J., Kondic, L. On the breakup of fluid films of finite and infinite extent. *Phys. Fluids* **19**, 072107 (2007).
- [15] Huppert, H.E. The propagation of two-dimensional and axisymmetric viscous gravity currents over a rigid horizontal surface. *J. Fluid Mech.* **121**, 43-58 (1982).
- [16] Diez, J.A., Kondic, L., Bertozzi, A. Global models for moving contact lines. *Phys. Rev. E* **63**, 011208 (2001).
- [17] Tarakhan, L.M. Determination of the surface tension of 5CB liquid crystal by the pendant drop method. *Ukr. J. Phys.* **51**, 22-26 (2006).
- [18] Of course, quantities such as viscosity can also change dramatically with temperature; but with the Bond and capillary numbers fixed, viscosity does not enter the remaining parameters. The viscosity would, however, affect the wavenumber of any observed instability, but this effect is not studied.